Supplementary Information

Superoxide-driven autocatalytic dark production of hydroxyl radicals in the presence of complexes of natural dissolved organic matter and iron

Yihua Xiao[1, 2, *], Luca Carena[3], Marja-Terttu Näsi[1], Anssi V. Vähätalo[1]

[1] *Department of Biological and Environmental Science, University of Jyväskylä, 40014 Jyväskylä, Finland*
[2] *School of Environmental & Municipal Engineering, Qingdao University of Technology, 266033 Qingdao, China*
[3] *Dipartimento di Chimica, Università di Torino, Via Pietro Giuria 5, 10125 Torino, Italy*

This Supplementary Information contains:

Table S1. Composition of artificial lake water. The concentrations refer to the final concentrations in the beginning of the experiment.

	Final concentration ($\mu mol\ L^{-1}$)
Na_2SO_4	54
KCl	7.9
$MgCl_2 \cdot 2H_2O$	28.8
$CaCl_2 \cdot 2H_2O$	60
$MnSO_4 \cdot H_2O$	0.31
$NaHCO_3$	0.04
$Na_2SiO_3 \cdot 5H_2O$	82
$NaNO_3$	5.0
NH_4Cl	0.03
$C_3H_{17}Na_2O_6P \cdot 6H_2O$*	21

*β-glycerophosphate disodium salt hydrate

Table S2. Description of four fluorescence components identified by PARAFAC

Component	Excitation/Emission maxima (nm)	Description
Comp 1	240(310)/415	Humic-like material with low molecular weight and aromaticity, common in marine environment but is also widely found in (boreal) freshwater, originated from biological activity (Coble et al., 1998; Gu et al., 2018; Kothawala et al., 2014; Zhang et al., 2009)
Comp 2	240(350)/459	Terrestrially-derived humic-like material with high molecular weight and aromaticity, is widely found but highest in forested environments and wetlands (Coble et al., 1990; Kothawala et al., 2014; Parlanti et al., 2000)
Comp 3	325/453	7OH-coumarin (Louit et al., 2005)
Comp 4	280/333	Tryptophan-like amino acid, free or bound on proteins indicating more degraded materials (Cory et al., 2005; Kothawala et al., 2014; Stedmon et al., 2003)

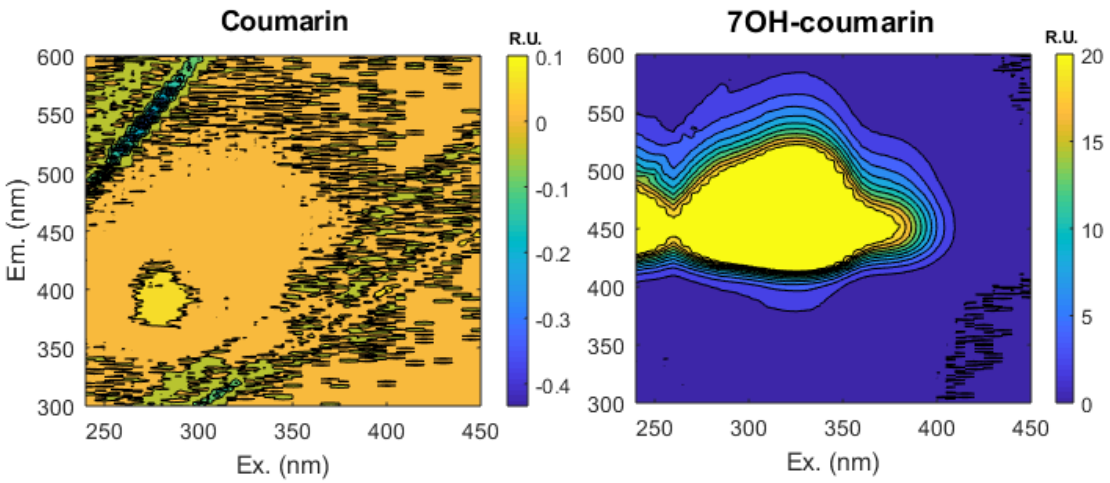

Figure S1. Excitation emission matrices for coumarin (left, 10 µmol L^{-1}) and 7OH-coumarin (right, 10 µmol L^{-1}). Note that the fluorescence of coumarin (given in units relative to the Raman of H_2O; R.U.) is nearly negligible

Text SI: Calculations on the $O_2^{\bullet-}$ disproportionation and DOM-Fe(III) reduction by $O_2^{\bullet-}$ in treatment of "Fe + KO_2"

This section will evaluate the reactions of superoxide ($O_2^{\bullet-}$) in the beginning of treatment "Fe + KO_2" containing 20 µmol L^{-1} DOM-Fe(III) and artificial lake water (Table S1). The Scheme SI-1 shows that $O_2^{\bullet-}$ can be either reduced to H_2O_2 or oxidized to O_2 (Fujii & Otani, 2017). Disproportionation can convert $O_2^{\bullet-}$ to H_2O_2 either spontaneously or though the catalysis by reduced metals or DOM, marked collectively as X_{red} in Scheme SI-1. Alternatively, oxidized DOM or metals (X_{ox}) can oxidize $O_2^{\bullet-}$ to O_2 (Scheme SI-I).

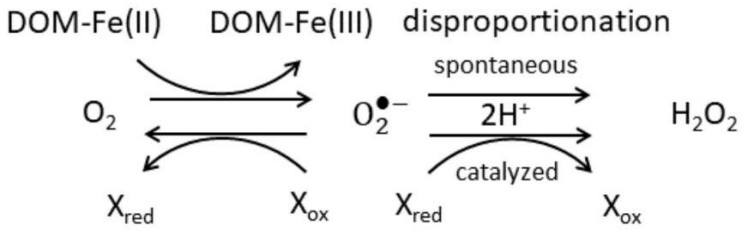

Scheme SI-1. Possible fates of superoxide in the treatment "Fe + KO_2" (modified from Fujii & Otani, 2017). X_{red} and X_{ox} refer to reduced and oxidized forms of metals or DOM.

In this study, the hydroxyl radical ($^{\bullet}OH$) production was an order of magnitude higher in the "KO_2 + Fe" treatment with DOM-Fe(III) than in the "KO_2" treatment with DOM alone. This finding suggests that the reaction of $O_2^{\bullet-}$ with DOM-Fe(III) (from X_{ox} to X_{red} in Scheme SI-1) played a major role in the production of $^{\bullet}OH$. Artificial lake water contained 0.31 µmol L^{-1} Mn(II) (i.e., X_{red} in Scheme SI-1), which can catalyze disproportionation of $O_2^{\bullet-}$ to H_2O_2 in addition to bimolecular disproportionation. One should notice that disproportionation requires also H^+ (Scheme SI-1), and thus the process is sensitive to pH. In this study, the introduction of KO_2 in 0.05 mol L^{-1} NaOH solution resulted in 13 µmol L^{-1} $O_2^{\bullet-}$ concentration but at the same time increased the pH of artificial lake water to 12.2. The calculations below indicate that at pH 12.2 the rate of disproportionation was negligible sink compared to DOM-Fe(III).

(1) Disproportionation of superoxide and hydroperoxy radical

The conjugate acid of $O_2^{\bullet-}$, hydroperoxy radical ($HO_2^{\bullet}$) forms when a superoxide anion ($O_2^{\bullet-}$) accepts a hydrogen ion:

$HO_2^{\bullet} \rightleftarrows O_2^{\bullet-} + H^+$ (Eq. SI-1).

For the equation of 1:

$K_{HO2} = [O_2^{\bullet-}]\,[H^+]/[HO_2^{\bullet}]$,

the equilibrium constant, K_{HO2}, is 1.6×10^{-5} L mol^{-1} (Bielski et al., 1985).

Spontaneous disproportionation of $HO_2^\bullet$ and $O_2^{\bullet-}$ to H_2O_2 and molecular O_2 can proceed either through:

$HO_2^\bullet + HO_2^\bullet \rightarrow H_2O_2 + O_2$ (Eq. SI-2)

with a second order rate constant, $k_2 = 8.3 \times 10^5$ L mol^{-1} s^{-1} (Bielski et al. 1985) or through:

$HO_2^\bullet + O_2^{\bullet-} + H_2O \rightarrow H_2O_2 + O_2 + OH^-$ (Eq. SI-3)

with a second order rate constant, $k_3 = 9.7 \times 10^7$ L mol^{-1} s^{-1} (Bielski et al., 1985).

Because $HO_2^\bullet$ is in an equilibrium with $O_2^{\bullet-}$ (Eq. SI-1), it is convenient to examine their concentrations together: $O_2^* = HO_2^\bullet + O_2^{\bullet-}$. In this case, the two separate disproportionation reactions can be presented together as:

$O_2^* + O_2^* + 2H^+ \rightarrow H_2O_2 + O_2$ (Eq. SI-4),

where the second order rate constant, k_4, can be calculated with the combination of k_2 and k_3 accounting for the equilibrium between $O_2^{\bullet-}$ and $HO_2^\bullet$ (Eq. SI-1):

$k_4 = (k_2 + k_3 (K_{HO2}/[H^+])) (1 + K_{HO2}/[H^+])^{-2}$ (Bielski et al., 1985).

The formation rate of H_2O_2 or molecular O_2 (mol L^{-1} s^{-1}) through disproportionation is:

$R_{H2O2,O2} = k_4 [O_2^*][O_2^*]$ (Eq. SI-5)

The rate of O_2^* consumption (mol L^{-1} s^{-1}) is:

$R_{O2*} = -2k_4 [O_2^*][O_2^*]$ (Eq. SI-6)

The temporal kinetics of O_2^* concentration (mol L^{-1}) can be described as:

$[O_2^*] = [O_2^*]_0/(1 + 2k_4 [O_2^*]_0 t)$ (Eq. SI-7)

where $[O_2^*]_0$ refers to the initial concentration of O_2^*.

and the half-life of O_2^* (s) is:

$t_{½,O2*} = (2k_4 [O_2^*]_0)^{-1}$ (Eq. SI-8)

At pH 12.2, $k_4 = 3.83$ L mol^{-1} s^{-1} and the half-life of the introduced O_2^* through disproportionation was 10054 s (= 2.79 hours) when calculated according to Eq. SI-8.

Manganese can react with superoxide at fast rate:

$Mn(II) + O_2^{\bullet-} \rightarrow MnO_2^+$ (Eq. SI-9)

and in this study convert 0.31 µmol L^{-1} (or 2.4% of introduced KO_2) into manganous superoxide (Wuttig et al., 2013). In seawater, MnO_2^+ behaves like $O_2^{\bullet-}$ and its major fate is disproportionation (Wuttig et al., 2013). At pH 12.2 of present study, the rate of disproportionation of MnO_2^+ is slow, if it behaves like $O_2^{\bullet-}$ (see above). Instead, MnO_2^+ is expected to form an equilibrium with Mn(II) and $O_2^{\bullet-}$ (Wuttig et al., 2013):

$MnO_2^+ \rightleftarrows Mn(II) + O_2^{\bullet-}$ (Eq. SI-10)

and $O_2^{\bullet-}$ will be eventually consumed by DOM-Fe(III) at pH 12.2 in the beginning of the "KO_2 + Fe" treatment.

(2) Reduction of DOM-Fe(III) by $O_2^{\bullet-}$

The reduction of DOM-Fe(III) by $O_2^{\bullet-}$ can be expressed as,

$DOM\text{-}Fe(III) + O_2^{\bullet-} \rightarrow DOM\text{-}Fe(II) + O_2$ (Eq. SI-11a).

The rate of superoxide consumption, DOM-Fe(III) loss and DOM-Fe(II) formation can be calculated as:

$rate = k_{11} [O_2^*] [DOM\text{-}Fe(III)]$ (Eq. SI-11b).

The second-order rate constant for the reaction SI-11 (k_{11} = 2.8 × 10^5 L mol^{-1} s^{-1}) has been determined at pH 8 using Suwannee River fulvic acid (SRFA) as a source of DOM (Garg et al., 2007). Using k_{11} = 2.8 × 10^5 L mol^{-1} s^{-1}, the reaction Eq. SI-11 consumed $O_2^{\bullet-}$ and produced 13 µmol DOM-Fe(II) within about two seconds after the introduction of KO_2.

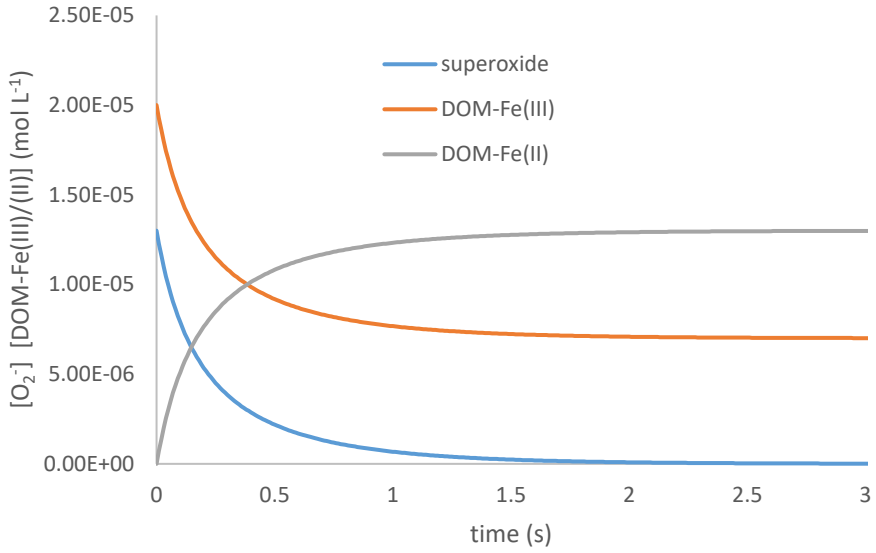

Figure SI-1. Calculated (Eq. SI-11) concentrations of superoxide (O_2^-), DOM-Fe(III) and DOM-Fe(II) in the beginning of "Fe + KO_2" treatment at pH 12.2.

3) The Fenton process in the beginning of experiment after the adjustment of pH to 5

After the introduction of KO_2 and rapid reduction of DOM-Fe(III) by $O_2^{\bullet-}$, the pH of artificial lake water was adjusted to 5. Under those conditions, the concentration of superoxide was initially negligible, but the water contained 13 µmol L^{-1} DOM-Fe(II) (Figure SI-1). The artificial lake water was in contact with atmosphere and contained 264 µmol L^{-1} dissolved O_2 according to the solubility of O_2 to fresh water at +25°C.

The oxidation of DOM-Fe(II) can lead to the production of $^{\bullet}OH$ through the following sequence of reactions.

Dissolved O_2 can oxidize DOM-Fe(II):

$$\text{DOM-Fe(II)} + O_2 \rightarrow \text{DOM-Fe(III)} + O_2^* \qquad \text{(Eq. SI-12)}$$

and produce O_2^* with k_{12} = 100 L mol^{-1} s^{-1} determined for SRFA (Garg et al., 2007). The loss of DOM-Fe(II) through Eq. SI-12 is calculated in Figure SI-2a.

DOM-Fe(II) can also dissociate:

$$\text{DOM-Fe(II)} \rightarrow \text{DOM} + \text{Fe(II)} \qquad \text{(Eq. SI-13)}$$

with $k_{13} = 8 \times 10^{-4}$ s^{-1} (Garg et al., 2007). Immediately after the pH adjustment to 5, the calculated rate of dissociation (1.04×10^{-8} mol L s^{-1}; Eq. SI-13) is an order of magnitude

lower than the oxidation of DOM-Fe(II) by O_2 (3.6×10^{-7} mol L s^{-1}; Eq. SI-12). This indicates that Eq. SI-12 was primarily responsible for the production of O_2^* and for simplicity the dissociation of DOM-Fe(II) is omitted in kinetic modelling presented in Figure SI-2.

At pH 5, the spontaneous disproportionation of O_2^* (Eq. SI-4; $k_4 = 2.3 \times 10^7$ L mol^{-1} s^{-1}) leads to a fast production of H_2O_2 (Figure SI-2a). DOM-Fe(II) reacts faster with H_2O_2 (Eq. SI-14; $k_{14} = 1.75 \times 10^4$ L mol^{-1} s^{-1}) (Pignatello et al., 2006) than with O_2 (Eq. SI-12):

$$\text{DOM-Fe(II)} + H_2O_2 \rightarrow \text{DOM-Fe(III)} + {}^{\bullet}OH + OH^- \qquad \text{(Eq. SI-14)}$$

and produces hydroxyl radicals (Figure SI-2b). In the beginning of experiment, the calculated maximum rate of $^{\bullet}OH$ (1.05×10^{-9} mol L^{-1} s^{-1}) is similar to the measured rate of $^{\bullet}OH$ production ($R_f^{\bullet OH}(t_0)$ $=1.14 \times 10^{-9}$ mol L^{-1} s^{-1}; Figure 4d).

The simple kinetic model (Figure SI-2) can explain the initial rate of $^{\bullet}OH$ production in "Fe + KO_2" treatment, but it fails to describe the later kinetics of $^{\bullet}OH$ production and the cumulative amounts of produced $^{\bullet}OH$ (Figure 4d; 104 µmol L^{-1} $^{\bullet}OH$ in 168 h, Table 2). The simple kinetic model (Figure SI-2) predicts that the formation of $^{\bullet}OH$ stops in about three minutes, and produces cumulatively 3.8 µmol L^{-1} of $^{\bullet}OH$ with a final residual concentration of 0.8 µmol L^{-1} H_2O_2. The stoichiometry of $^{\bullet}OH$ production in the kinetic model (Figure SI-2) approximates iron-catalyzed Haber-Weiss process (Rush & Bielski, 1985):

$$HO_2^{\bullet} + H_2O_2 \xrightarrow{\text{Fe(II)/Fe(III)}} {}^{\bullet}OH + H_2O + O_2 \qquad \text{(Eq. SI-15a).}$$

When the formation of H_2O_2 through disproportionation (Eq. SI-4) is included in Eq. SI-15a, it becomes:

$$3\ HO_2^{\bullet} \xrightarrow{\text{Fe(II)/Fe(III)}} {}^{\bullet}OH + H_2O + 2\ O_2 \qquad \text{(Eq. SI-15b),}$$

The reaction Eq. SI-15 represents the theoretical maximum yield of $^{\bullet}OH$ ($^{\bullet}OH$/ 3 O_2^*) from superoxide through Fe catalysis, which is 4.3 µmol L^{-1} of $^{\bullet}OH$ from 13 µmol L^{-1} O_2^*. As the measured yield of $^{\bullet}OH$ (104 µmol L^{-1} $^{\bullet}OH$ in 168 h, Table 2) was 24-fold higher than the theoretical yield from $O_2^{\bullet-}$ (4.3 µmol L^{-1} $^{\bullet}OH$, Eq, SI-15b), the production of $^{\bullet}OH$ in the "Fe + KO_2" treatment must have included an autocatalytic process.

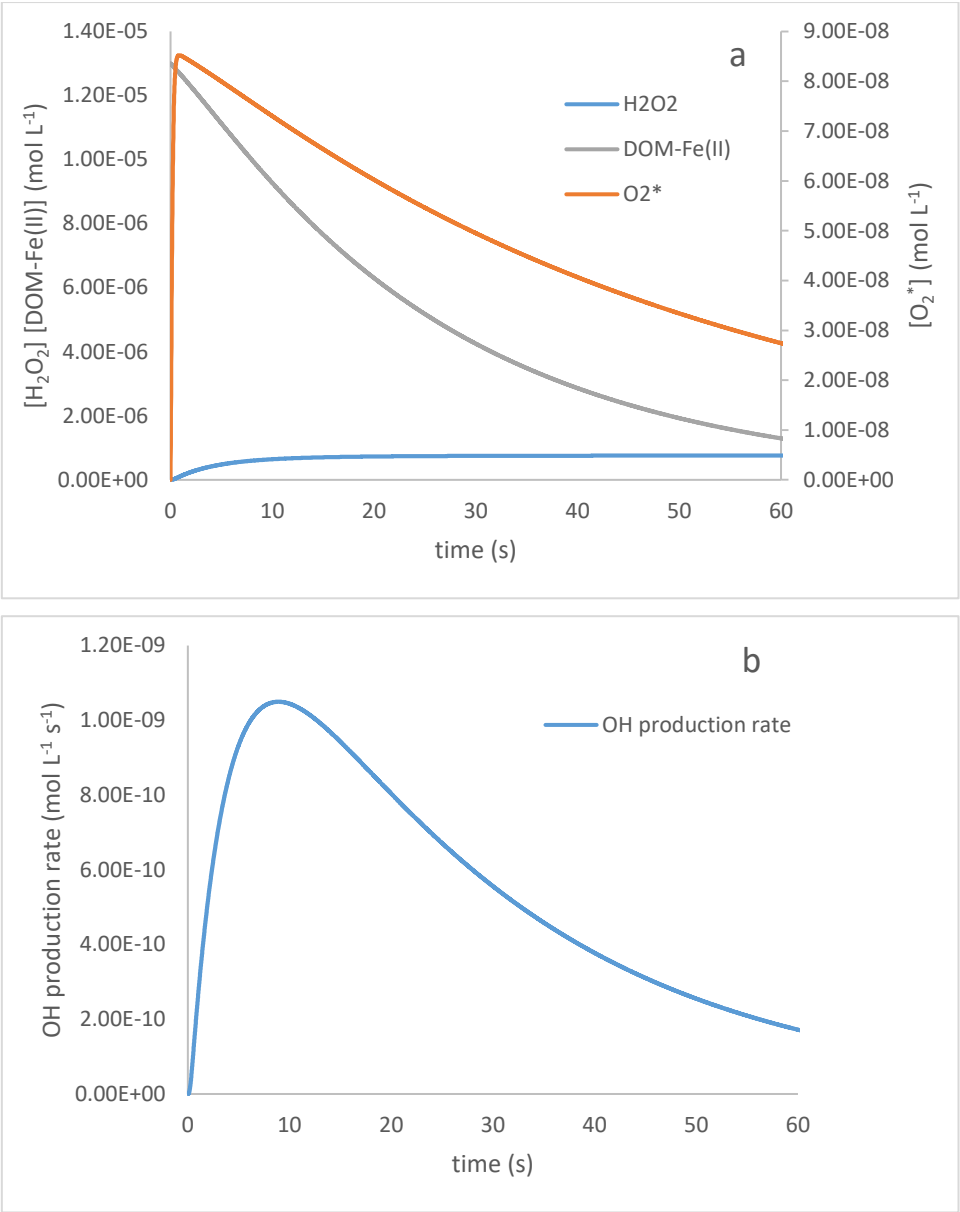

Figure SI-2. The calculated concentrations of DOM-Fe(II), H_2O_2 and O_2^* (a) and the production rate of hydroxyl radicals. The calculations on the oxidation of DOM-Fe(II) (Eq. SI-12), disproportionation of O_2^* (Eq. SI-4) and the Fenton reaction (Eq. SI-14).

Text SII: HPLC analysis for detecting coumarin and 7OH-coumarin

The HPLC system was a Shimadzu LC-30AD equipped with SIL-30AC autosampler, CTO-20AC column oven (set at 30 °C), DGU-20A5R degassing unit, SPD-M20A PDA detector and RF-20A XS fluorescence detector. Chromatographic runs were carried out with a reverse phase chromatography column Bridge Columns XBridge™ C18 (2.5 μm) in a gradient mode with a mixture of two eluents (A and B). Eluent A was 0.3% acetic acid with 99.7% ultrapure water, while B was 100% acetonitrile. The flow rate was 0.3 mL min^{-1}. The relevant elution gradients were: 10% of B from 0 to 0.5 min, then linear gradient to 45% of B from 0.5 to 6 min, followed by a fast linear gradient to 75% of B for 6–6.5 min; 75% of B was then kept from 6.5 to 9 min and then followed by a linear gradient to the initial condition 10% of B at 9.5 min, the same gradient was kept until 12.5 min for stabilizing the system. The injection volume was 5 μL. The first sample was run two times to make sure the gradient solvent was fully stabilized in the system. The retention times were 5.23 min for coumarin and 3.64 min for 7OH-coumarin. Quantification of the two compounds was carried out by means of the PDA detector for coumarin (absorption wavelength = 280 nm) and of the fluorescence detector for 7OH-coumarin (excitation wavelength = 320 nm; emission wavelength = 450 nm).

Text SIII: Calculating the cumulative production of •OH radicals by using the transformation of coumarin into 7-hydroxycoumarin as a •OH probe reaction

The cumulative production of •OH radicals per unit of volume over a defined time ($[^{\bullet}OH]_{\Sigma}$, mol L^{-1}) was described as a definite integral over time:

$$[^{\bullet}OH]_{\Sigma} = \int_{t_0}^{t_1} R_f^{\bullet OH}(t)\, dt \qquad (Eq.\,SIII-1),$$

where t_0 and t_1 represent the time in the beginning of experiment and at the selected time t_1, respectively, and $R_f^{\bullet OH}(t)$ is the formation rate of •OH radicals at time t (mol L^{-1} s^{-1}).

$R_f^{\bullet OH}(t)$ was calculated from the scavenging rate of hydroxyl radicals. Because •OH radicals react with their scavengers almost at diffusion-controlled rates, the total scavenging rate of •OH at time t approximates $R_f^{\bullet OH}(t)$.When the formation and scavenging rates are nearly the same, the •OH concentration at time t approximates a steady-state. In the experimental solutions, the scavengers (see Scheme SIII-1) set the steady-state concentration of •OH radicals ($[^{\bullet}OH]_{s.s.}$) to:

$$[^{\bullet}OH]_{s.s.} = \frac{R_f^{\bullet OH}(t)}{k'_{Scav} + k_{Cou}^{\bullet OH}[Cou]_t + k_{7OHCou}^{\bullet OH}[7OHCou]_t} \qquad (Eq.\,SIII-2),$$

where $[Cou]_t$ and $[7OHCou]_t$ are the concentrations of coumarin and 7-hydroxycoumarin (7OH-coumarin) at time t, respectively (Figures SIII-1&2), and k'_{Scav} represents scavenging by the artificial lake water (Table SIII-1). k'_{Scav} accounted for the major scavengers of •OH in the artificial lake water: DOM (DOC = 11.35 mg C L^{-1}), chloride (*vide infra* for its concentration) and bicarbonate anions (4×10^{-6} mol L^{-1}), and thus $k'_{Scav} = k_{DOM}^{\bullet OH}DOC + k_{Cl^-}^{\bullet OH}[Cl^-] + k_{HCO_3^-}^{\bullet OH}[HCO_3^-]$. The modeling used the initial concentrations of Cl^- and HCO_3^- (Table SIII-1). In terms of DOM, we assumed that the reactions between hydroxyl radicals and DOM resulted primarily in the transformation products that reacted with hydroxyl radical like reported for DOM in literature (Westerhoff et al. 2007). Therefore, we used the initial concentrations of DOM in the calculations (Table SIII-1). The modeling also ignored the reactions of •OH radicals with the different coumarin degradation byproducts (P_2 and P_3 Scheme SIII-1), as well as those with the iron species, because we did not measure the temporal

variation of these compounds. However, this should not cause significant modeling errors, because these constituents had lower concentrations than the major scavenger DOM, making negligible their role in the total •OH radicals scavenging. The reaction rate constants were from literature: $k_{Cou}^{\bullet OH}$ = 5.6×10^9 L mol^{-1} s^{-1}; $k_{7OHCou}^{\bullet OH}$ = 6.1×10^9 L mol^{-1} s^{-1}; $k_{DOM}^{\bullet OH}$ = 1.9×10^4 L mg C^{-1} s^{-1}; $k_{HCO_3^-}^{\bullet OH}$ = 8.5×10^6 L mol^{-1} s^{-1} (Burgos Castillo et al., 2018; Buxton et al., 1988; Payá et al., 1992; Westerhoff et al., 2007). The value of $k_{Cl^-}^{\bullet OH}$ took into account the pH dependence of the •OH scavenging kinetics by Cl$^-$ (see Scheme SIII-1). At pH 2, the reaction between •OH and Cl$^-$ yields hypochlorous acid anion radicals (HOCl$^{\bullet-}$, k_1 = 4.3×10^9 L mol^{-1} s^{-1}, Buxton et al., 1988). In acidic conditions the protonation of HOCl$^{\bullet-}$ induces the formation of a chlorine atom (Cl$^\bullet$) and a water molecule (k_2 = 2.1×10^{10} L mol^{-1} s^{-1}, Jayson et al., 1973) making Cl$^-$ as an actual sink for •OH. At circumneutral and basic pH values, HOCl$^{\bullet-}$ dissociates back to •OH and Cl$^-$ (k_{-1} = 6.1×10^9 s^{-1}, Jayson et al., 1973). By considering these reactions and by reasonably applying the steady-state to the HOCl$^{\bullet-}$ concentration, the pH dependence of $k_{Cl^-}^{\bullet OH}$ can be described as $k_1k_2$10^{-pH}(k_{-1} + $k_2$10^{-pH})$^{-1}$ (see also the paper by Jayson et al., 1973). Therefore, $k_{Cl^-}^{\bullet OH}$ ~ 1.5×10^5 L mol^{-1} s^{-1} at pH 5. Chloride concentrations used in the model took into account all the Cl$^-$ sources (i.e. artificial lake water, $FeCl_3$, and HCl for the titration procedures) and were 1.84×10^{-4} mol L^{-1} ("control"), 7.4×10^{-3} mol L^{-1} ("Fe"), 1.62×10^{-2} mol L^{-1} ("KO_2") and 2.12×10^{-2} mol L^{-1} ("Fe+ KO_2").

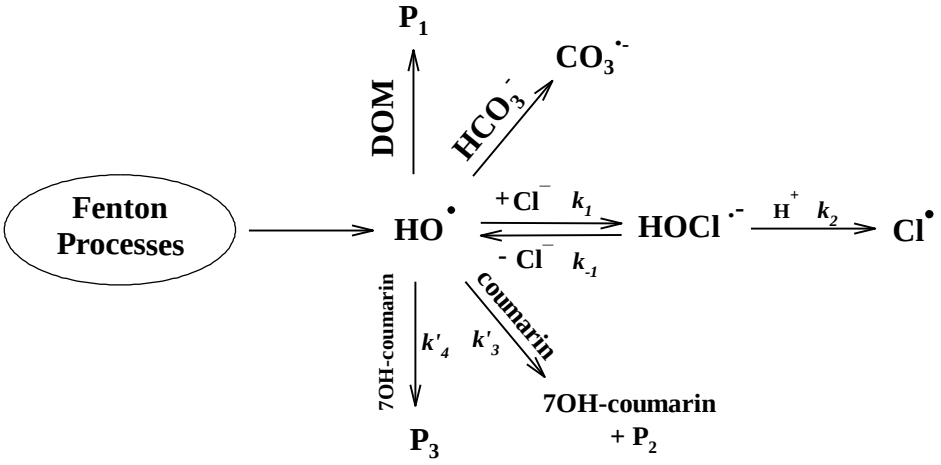

Scheme SIII-1. Simplified reaction scheme describing the formation and the scavenging pathways of •OH radicals in the experiment. 'P_i' refers to a general byproduct(s).

The transformation rate of 7OH-coumarin, $R_{\Delta}^{7OHCou}(t)$, was a master variable in the assessment of $R_f^{\bullet OH}(t)$. $R_{\Delta}^{7OHCou}(t)$ was defined as the difference between the formation rate (coumarin + $^{\bullet}$OH reaction) and the decay rate (7OH-coumarin + $^{\bullet}$OH reaction):

$$R_{\Delta}^{7OHCou}(t) = [^{\bullet}OH]_{s.s.}\{\eta_{7OHCou}^{Cou} k_{Cou}^{\bullet OH}[Cou]_t - k_{7OHCou}^{\bullet OH}[7OHCou]_t\} \qquad (Eq.SIII-3),$$

where η_{7OHCou}^{Cou} = 0.047 is the yield for the formation of 7OH-coumarin from the coumarin + $^{\bullet}$OH reaction (Burgos Castillo et al., 2018). By substituting Eq. SIII-2 in Eq. SIII-3, one obtains:

$$R_{\Delta}^{7OHCou}(t) = \frac{R_f^{\bullet OH}(t)\{\eta_{7OHCou}^{Cou} k_{Cou}^{\bullet OH}[Cou]_t - k_{7OHCou}^{\bullet OH}[7OHCou]_t\}}{k'_{Scav} + k_{Cou}^{\bullet OH}[Cou]_t + k_{7OHCou}^{\bullet OH}[7OHCou]_t} \qquad (Eq.SIII-4)$$

By rearranging Eq. SIII-4, the expression for $R_f^{\bullet OH}(t)$ will be:

$$R_f^{\bullet OH}(t) = \frac{R_{\Delta}^{7OHCou}(t)\{k'_{Scav} + k_{Cou}^{\bullet OH}[Cou]_t + k_{7OHCou}^{\bullet OH}[7OHCou]_t\}}{\{\eta_{7OHCou}^{Cou} k_{Cou}^{\bullet OH}[Cou]_t - k_{7OHCou}^{\bullet OH}[7OHCou]_t\}} \qquad (Eq.SIII-5)$$

$R_{\Delta}^{7OHCou}(t)$ was assessed as the first derivative ($d[7OHCou]_t dt^{-1}$) of a function that described the temporal development of $[7OHCou]_t$ in the treatments. In order to determine $d[7OHCou]_t dt^{-1}$, a kinetic equation SIII-6 (the curves in Figure SIII-1) was fitted on the measured concentrations of 7OH-coumarin during the course of experiment (the squares in Figure SIII-1).

$$[7OHCou]_t = \frac{k'_3 a}{k'_4 - k'_3}(e^{-k'_3 t} - e^{-k'_4 t}) \qquad (Eq.SIII-6)$$

where k'_3 and k'_4 are the pseudo-first order rate constants for the reactions $Cou \rightarrow 7OHCou$ and $7OHCou \rightarrow P_3$, respectively (Scheme SIII-1), and a is a concentration parameter. The values of $R_{\Delta}^{7OHCou}(t)$ were graphically computed as the slope of the tangent line to the curves shown in Figure SIII-1 at several reaction times shown in Figure 4.

For the calculation of $R_f^{\bullet OH}(t)$, Eq. SIII-5 received the values of $R_{\Delta}^{7OHCou}(t)$, $[7OHCou]_t$ (Figure SIII-1) and $[Cou]_t$ (Figure SIII-2) at the selected times (the reaction times in Figure 4).

The decreasing trend in $R_f^{\bullet OH}(t)$ at the selected times (the squares in Figure 4) was described by an exponential equation (the curves in Figure 4):

$$R_f^{\bullet OH}(t) = R_f^{\bullet OH}(t_0)\, e^{-kt} \qquad (Eq.\ \text{SIII-7}),$$

where $R_f^{\bullet OH}(t_0)$ is the rate of hydroxyl radicals formation in the beginning of experiment (nmol L^{-1} s^{-1}) and k (s^{-1}) describes the degree of exponential loss in $R_f^{\bullet OH}(t)$. In the "Fe+KO_2"-treatment, $R_f^{\bullet OH}(t)$ decreased initially exponentially but plateaued later (Figure 4d) and therefore the kinetics was described by:

$$R_f^{\bullet OH}(t) = R_f^{\bullet OH}(t_0)\, e^{-kt} + R_f^{\bullet OH}\left(t_{plateau}\right) \qquad (Eq.\ \text{SIII-8}),$$

where $R_f^{\bullet OH}\left(t_{plateau}\right)$ is the rate at the plateau. Table SIII-1 shows the values of the relevant parameters of Eq. SIII-7&8.

Finally, the $[^{\bullet}OH]_{\Sigma}$ values were calculated by solving the integral of these fitting functions as in Eq. SIII-1.

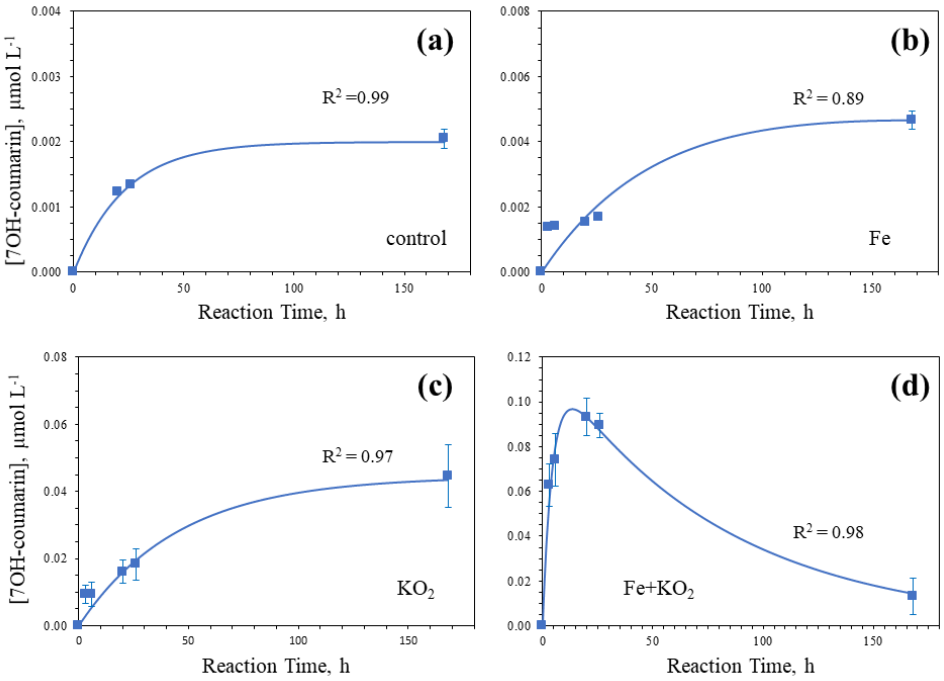

Figure SIII-1. The measured concentrations of 7-hydroxycoumarin (7OH-coumarin) (■) and the kinetic fitting on the measured data (blue lines). The error bars represent data standard deviations. The

R^2 parameter shows the goodness of the fit. See Eq. S6 for the general form of the fitting functions. Note, the differences in the scale of Y-axis among the panels.

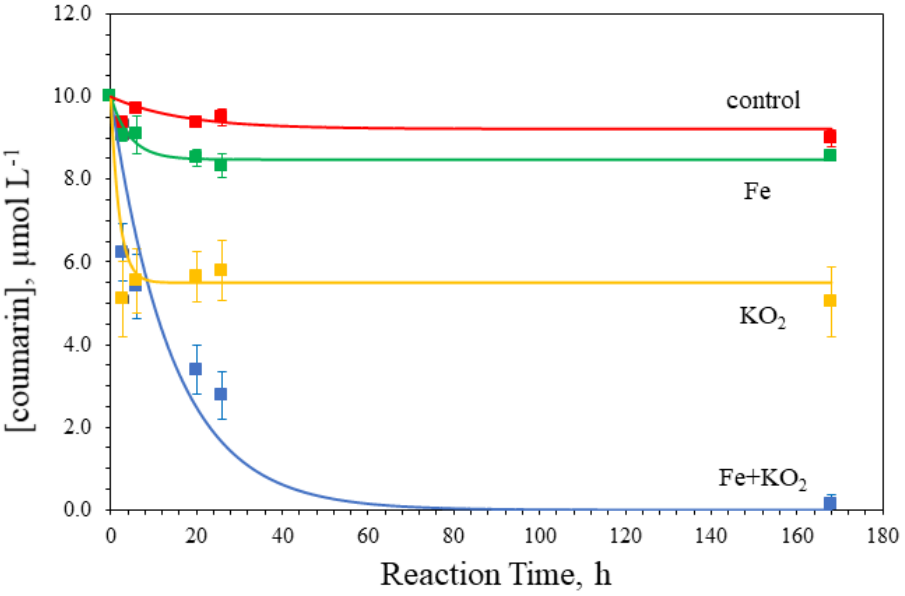

Figure SIII-2. Concentration profiles of coumarin observed in the different treatments. The error bars represent the standard deviations of the measured coumarin concentrations (squares). Data were fitted with the equation $[Cou]_t = C + A\exp(-Bt)$ (lines). In the case "Fe+KO_2", C = 0 (blue curve).

Table SIII-1. Fitting parameters obtained by interpolating the $R_f^{\bullet OH}(t)$ data with Eq. SIII-7 & SIII-8. The R^2 value shows the goodness of the fit.

Treatment	$\boldsymbol{R_f^{\bullet OH}(t_0)}$, **nmol L^{-1} s^{-1}**	$\boldsymbol{k}$, **s^{-1}**	$\boldsymbol{R_f^{\bullet OH}(t_{plateau})}$, **nmol L^{-1} s^{-1}**	**R^2**
control	$(3.074\pm0.085)\times10^{-3}$	$(1.340\pm0.067)\times10^{-5}$	0	0.99
Fe	$(3.361\pm0.221)\times10^{-3}$	$(5.668\pm0.804)\times10^{-6}$	0	0.97
KO_2	$(3.894\pm0.225)\times10^{-2}$	$(3.454\pm0.466)\times10^{-6}$	0	0.95
Fe+KO_2	$(9.910\pm0.384)\times10^{-1}$	$(8.745\pm0.701)\times10^{-5}$	$(1.523\pm0.137)\times10^{-1}$	0.99

Text SIV: Modeling $O_2^{\bullet-}$ photoproduction in lake water.

Superoxide ($O_2^{\bullet-}$) photochemical production in surface waters can be related to the formation of hydrogen peroxide (H_2O_2) from irradiated chromophoric dissolved organic matter (CDOM). Indeed, H_2O_2 is photoproduced by CDOM through a mechanism that would involve the reduction of dioxygen (O_2) to superoxide $O_2^{\bullet-}$ by O_2-reducing intermediates that are generated by intramolecular electron transfer from CDOM short-lived excited states of electron donors (probably phenols) to ground-state acceptors (most likely quinone-like moieties) (Zhang et al., 2012). In the presence of a high content of electro-donating phenols, the excited triplet states of CDOM can be involved in $O_2^{\bullet-}$ photoproduction as well (Zhang et al., 2014). Then $O_2^{\bullet-}$ can undergo dismutation, which can occur via three main pathways: *(i)* uncatalyzed dismutation ($O_2^{\bullet-} + HO_2^{\bullet}$), *(ii)* DOM-catalyzed dismutation ('DOM' means dissolved organic matter) and *(iii)* dismutation catalyzed by organometallic compounds containing Fe, Cu and Mn (Goldstone & Voelker, 2000; Ma et al., 2019). Among these processes, the DOM-catalyzed dismutation of $O_2^{\bullet-}$ into $H_2O_2 + O_2$ can play the main scavenging role of $O_2^{\bullet-}$ in inland surface waters (Ma et al., 2019). As far as the stoichiometry of $O_2^{\bullet-}$ dismutation is concerned, previous works have determined the ratio H_2O_2:$O_2^{\bullet-}$ for different DOM type (Goldstone & Voelker, 2000; Powers & Miller, 2016), showing that the ratio should be ~0.5 for DOM typically occurring in inland waters, while it would decrease down to ~0.25 for seawater and open ocean (Powers & Miller, 2016). Here, we adopted the former values in order to model superoxide photoproduction in lake water.

By doubling the H_2O_2 photoproduction rate from irradiated CDOM (R_{H2O2}^{CDOM}), one can get the $O_2^{\bullet-}$ photoformation rate, $R_{O_2^{\bullet-}}^{CDOM} = 2R_{H2O2}^{CDOM} = 2\Phi_{H2O2}^{CDOM} P_{a,CDOM}$. Φ_{H2O2}^{CDOM} is the polychromatic apparent quantum yield (pAQY) of H_2O_2 formation from irradiated CDOM, while $P_{a,CDOM}$ is the total photon flux absorbed by CDOM (or photons absorption rate, Einstein L^{-1} s^{-1}). Φ_{H2O2}^{CDOM} has been measured by Zhang et al. (2012) for several DOM samples, such as Suwannee River humic and fulvic acids, a lignin-like material and a river water sample. The average value for these materials is ~5.9×10^{-4}. $P_{a,CDOM}$ is a function of the light absorption properties of CDOM, water depth and chemical composition, namely $P_{a,CDOM} = \int_{\lambda 1}^{\lambda 2} p^0(\lambda) \frac{Abs_\lambda^{CDOM}}{Abs_\lambda^{tot}} \left[1 - 10^{-Abs_\lambda^{tot}}\right] d\lambda$. Abs_λ^{tot} is the total absorbance of water that takes into account the water depth and the Lambert-Beer absorbance of the main light-absorbing species, Abs_λ^{CDOM} is the absorbance of CDOM and $p^0(\lambda)$ is the spectral solar photon flux (Einstein L^{-1} s^{-1} nm^{-1}). To

evaluate $P_{a,CDOM}$ one has to know all these parameters, which are particular features of the considered water body. The APEX software (*Aqueous Photochemistry of Environmentally occurring Xenobiotics*; Bodrato & Vione, 2014) allows to indirectly assess $P_{a,CDOM}$. Indeed, APEX models the direct and indirect photochemistry of water pollutants in well-mixed surface waters (e.g., Carena et al., 2017), such as the lake epilimnion during stratification in summertime, as well as the steady-state concentrations of the main *Photochemically Produced Reactive Intermediates* (PPRIs), namely hydroxyl and carbonate radicals ($HO^{\bullet}$ and $CO_3^{\bullet-}$, respectively), the excited triplet states of CDOM (^{3}CDOM*) and singlet oxygen ($^1O_2$).

To assess the PPRIs steady-state concentrations, APEX requires as input data the chemical and photochemical features of the water body, namely the photosensitizers concentration (NO_3^-, NO_2^- and CDOM, the latter quantified by means of the dissolved organic carbon DOC), the water absorption spectrum (which is computed based on the input DOC value) and the water depth. For the detailed description of the model, see the APEX User Guide available for free in Bodrato and Vione (2014). The software output data are averaged over the entire water column depth. $P_{a,CDOM}$ can be determined by modeling the steady-state concentration of ^{3}CDOM*, $[^3CDOM^*]_{s.s.} = \Phi_{3CDOM*}^{CDOM} P_{a,CDOM} (k_{3CDOM*})^{-1}$, where Φ_{3CDOM*}^{CDOM} = 1.28x10^{-3} is the ^{3}CDOM* formation pAQY and k_{3CDOM*} = 5x10^5 s^{-1} is the rate constant of the ^{3}CDOM* scavenging by the reaction with O_2 (that forms $^1O_2$). As a consequence, $R_{O_2^{\bullet-}}^{CDOM} = 2R_{H2O2}^{CDOM} = 2\Phi_{H2O2}^{CDOM} [^3CDOM^*]_{s.s.} k_{3CDOM*} (\Phi_{3CDOM*}^{CDOM})^{-1}$. Note that this equation refers to the direct photoproduction of $O_2^{\bullet-}$ upon sunlight absorption by CDOM. It does not take into account those reactions occurring in surface waters that indirectly photoproduce $O_2^{\bullet-}$ as an intermediate, such as, for example, the DOM photodegradation, the nitrate/nitrite photolysis, and the xenobiotics degradation. Moreover, note that here $R_{O_2^{\bullet-}}^{CDOM} \propto [^3CDOM^*]_{s.s.}$ is only due to $P_{a,CDOM}$ - evaluation purposes, and it does not mean that ^{3}CDOM* is mechanistically linked to $O_2^{\bullet-}$ photoproduction (Zhang et al., 2014; Zhang et al., 2012).

Figure SIV-1 shows $R_{O_2^{\bullet-}}^{CDOM}$ as a function of water depth and DOC. It must be pointed out that the $R_{O_2^{\bullet-}}^{CDOM}$ strongly depends upon O_2 concentration (Zhang et al., 2012). Unfortunately, APEX does not consider O_2 as an input variable and thus the results showed in Fig. SIV-1 are relevant for well oxygenated (saturated) waters.

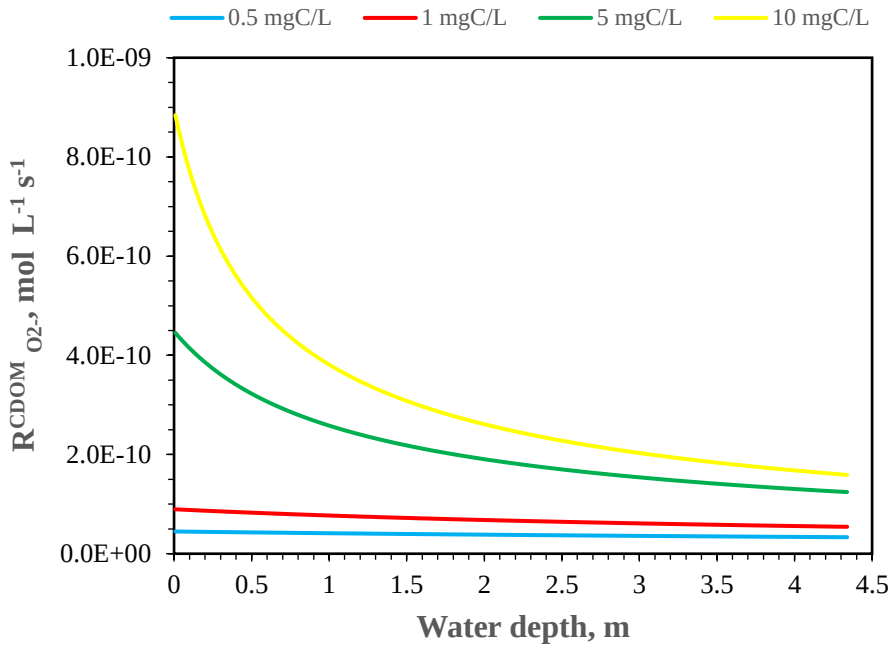

Figure SIV-1. Superoxide photoproduction rate in a temperate lake (45°N) as a function of water depth and DOC, during the 15th of July at 09 am or 03 pm. Other water chemical composition parameters were 1.0x10^{-4} mol L^{-1} NO_3^-, 1.0x10^{-6} mol L^{-1} NO_2^-, 1.0x10^{-3} mol L^{-1} alkalinity and pH 7. Note that the data are averaged over the entire water column.

The solar spectrum used for the modeling (i.e., $p^0(\lambda)$) refers to the Sun spectrum reaching the water surface on the 15th of July at mid-latitudes (45°N) at solar noon ± 3h, that is at 09 a.m. or 03 p.m., with 22 W m^{-2} UV irradiance. This is roughly representative of a daily average solar spectrum. Such a condition allows to define the Summer Sunny Day (SSD), which is the time unit adopted by APEX to describe, for instance, the photochemical half-life time of water pollutants. SSD = 10 h of continuous solar irradiation with 22 W m^{-2} UV irradiance.

By so doing, one can assess how many hours of solar irradiation are required to directly photoproduce 13 µmol $O_2^{\bullet-}$ L^{-1} in a lake, without considering the daily fluctuations of solar irradiance. $R_{O_2^{\bullet-}}^{CDOM}$ varied from 4.5x10^{-11} to 9x10^{-10} mol L^{-1} s^{-1} and, as a consequence, 13 µmol $O_2^{\bullet-}$ L^{-1} are photoproduced in a time interval ranging from ~4 h to ~8.5 SSD in the first meter of a lake (Fig. SIV-2). The modeled $R_{O_2^{\bullet-}}^{CDOM}$ for 0.5 and 1 mgC L^{-1} are quite similar to the superoxide formation rates that can be calculated from the H_2O_2 production rates measured by García et al. (2019) during lab irradiation of Andean shallow lakes with similar DOC values. However, these results can be considered as minimum limit values of superoxide photoproduction, because the ratio H_2O_2:$O_2^{\bullet-}$ could be lower than the adopted one (i.e., 0.5).

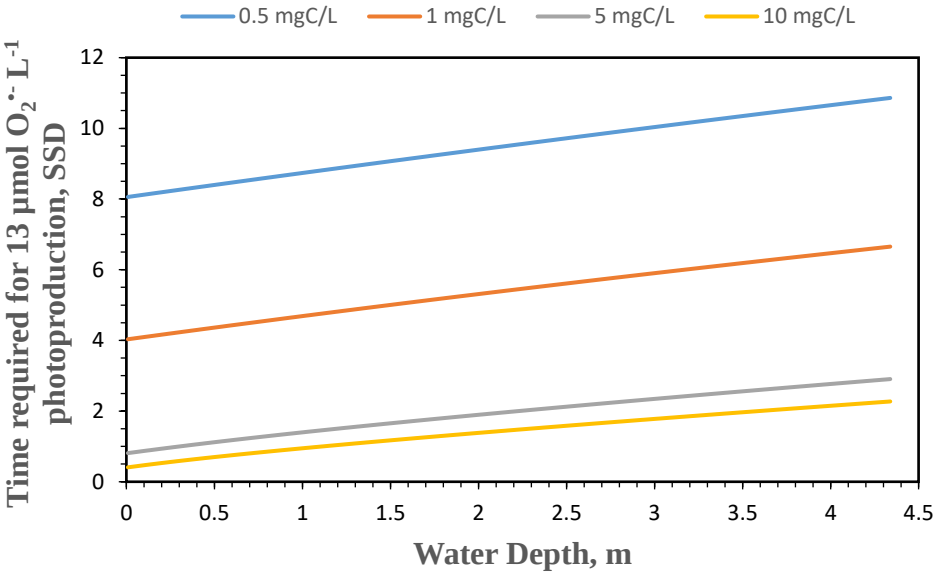

Figure SIV-2. Time required for 13 µmol $O_2^{\bullet-}$ L^{-1} photoproduction in a temperate lake (45°N) as a function of water depth and DOC, during the 15th of July at 09 am or 03 pm. Further water chemical composition parameters were $1.0x10^{-4}$ mol L^{-1} NO_3^-, $1.0x10^{-6}$ mol L^{-1} NO_2^-, $1.0x10^{-3}$ mol L^{-1} alkalinity and pH 7. Note that the data are averaged over the entire water column.

References

Bielski, B. H. J., Cabelli, D. E., & Arudi, R. L. (1985). Reactivity of HO2/O2– radicals in aqueous solution. *Journal of Physical Chemistry Reference Data*, *14*(4), 1041–1100.

Bodrato, M., & Vione, D. (2014). APEX (Aqueous Photochemistry of Environmentally occurring Xenobiotics): A free software tool to predict the kinetics of photochemical processes in surface waters. *Environmental Sciences: Processes and Impacts*, *16*(4), 732–740. https://doi.org/10.1039/c3em00541k

Burgos Castillo, R. C., Fontmorin, J. M., Tang Walter, Z., Xochitl, D. B., & Mika, S. (2018). Towards reliable quantification of hydroxyl radicals in the Fenton reaction using chemical probes. *RSC Advances*, *8*(10), 5321–5330. https://doi.org/10.1039/c7ra13209c

Buxton, G. V., Greenstock, C. L., Helman, W. P., & Ross, A. B. (1988). Critical Review of rate constants for reactions of hydrated electrons, hydrogen atoms and hydroxyl radicals (·OH/·O−in Aqueous Solution. *Journal of Physical and Chemical Reference Data*, *17*(2), 513–886. https://doi.org/10.1063/1.555805

Carena, L., Minella, M., Barsotti, F., Brigante, M., Milan, M., Ferrero, A., et al. (2017). Phototransformation of the Herbicide Propanil in Paddy Field Water. *Environmental Science & Technology*, *51*(5), 2695–2704. https://doi.org/10.1021/acs.est.6b05053

Coble, P. G., Green, S. A., Blough, N. V., & Gagosian, R. B. (1990). Characterization of dissolved organic matter in the Black Sea by fluorescence spectroscopy. *Nature*, *348*(6300), 432–435. https://doi.org/10.1038/348432a0

Coble, P. G., Del Castillo, C. E., & Avril, B. (1998). Distribution and optical properties of CDOM in the Arabian Sea during the 1995 Southwest Monsoon. *Deep Sea Research Part II: Topical Studies in Oceanography*, *45*(10–11), 2195–2223. https://doi.org/10.1016/S0967-0645(98)00068-X

Cory, R. M., McKnight, D. M., And, R. M. C., & McKnight, D. M. (2005). Fluorescence spectroscopy reveals ubiquitous presence of oxidized and reduced quinones in dissolved organic matter. *Environmental Science & Technology*, *39*(21), 8142–8149. https://doi.org/10.1021/ES0506962

Fujii, M., & Otani, E. (2017). Photochemical generation and decay kinetics of superoxide and hydrogen peroxide in the presence of standard humic and fulvic acids. *Water Research*, *123*, 642–654. https://doi.org/10.1016/j.watres.2017.07.015

García, P. E., Queimaliños, C., & Diéguez, M. C. (2019). Natural levels and photo-production rates of

hydrogen peroxide (H2O2) in Andean Patagonian aquatic systems: Influence of the dissolved organic matter pool. *Chemosphere*, 550–557. https://doi.org/10.1016/j.chemosphere.2018.10.179

Garg, S., Rose, A. L., & Waite, T. D. (2007). Superoxide mediated reduction of organically complexed iron(III): Comparison of non-dissociative and dissociative reduction pathways. *Environmental Science & Technology*, *41*(9), 3205–3212. https://doi.org/10.1021/ES0617892

Goldstone, J. V., & Voelker, B. M. (2000). Chemistry of superoxide radical in seawater: CDOM associated sink of superoxide in coastal waters. *Environmental Science & Technology*, *34*(6), 1043–1048. https://doi.org/10.1021/es9905445

Gu, C., Wang, J., Guo, M., Sui, M., Lu, H., & Liu, G. (2018). Extracellular degradation of tetrabromobisphenol A via biogenic reactive oxygen species by a marine Pseudoalteromonas sp. *Water Research*, *142*, 354–362. https://doi.org/10.1016/j.watres.2018.06.012

Jayson, G. G., Parsons, B. J., & Swallow, A. J. (1973). Some simple, highly reactive, inorganic chlorine derivatives in aqueous solution. Their formation using pulses of radiation and their role in the mechanism of the Fricke dosimeter. *Journal of the Chemical Society, Faraday Transactions 1: Physical Chemistry in Condensed Phases*, *69*, 1597–1607. https://doi.org/10.1039/F19736901597

Kothawala, D. N., Stedmon, C. A., Muller, R. A., Weyhenmeyer, G. A., Köhler, S. J., & Tranvik, L. J. (2014). Controls of dissolved organic matter quality: evidence from a large-scale boreal lake survey, *20*, 1101–1114. https://doi.org/10.1111/gcb.12488

Louit, G., Foley, S., Cabillic, J., Coffigny, H., Taran, F., Valleix, A., et al. (2005). The reaction of coumarin with the OH radical revisited: Hydroxylation product analysis determined by fluorescence and chromatography. *Radiation Physics and Chemistry*, *72*(2–3), 119–124. https://doi.org/10.1016/j.radphyschem.2004.09.007

Ma, J., Zhou, H., Yan, S., & Song, W. (2019). Kinetics studies and mechanistic considerations on the reactions of superoxide radical ions with dissolved organic matter. *Water Research*, *149*, 56–64. https://doi.org/10.1016/J.WATRES.2018.10.081

Parlanti, E., Wörz, K., Geoffroy, L., & Lamotte, M. (2000). Dissolved organic matter fluorescence spectroscopy as a tool to estimate biological activity in a coastal zone submitted to anthropogenic inputs. *Organic Geochemistry*, *31*(12), 1765–1781. https://doi.org/10.1016/S0146-6380(00)00124-8

Payá, M., Halliwell, B., & Hoult, J. R. S. (1992). Interactions of a series of coumarins with reactive oxygen species. Scavenging of superoxide, hypochlorous acid and hydroxyl radicals. *Biochemical Pharmacology*, *44*(2), 205–214. https://doi.org/10.1016/0006-2952(92)90002-Z

Pignatello, J. J., Oliveros, E., & MacKay, A. (2006). Advanced oxidation processes for organic contaminant destruction based on the fenton reaction and related chemistry. *Critical Reviews in Environmental Science and Technology*, *36*(1), 1–84. https://doi.org/10.1080/10643380500326564

Powers, L. C., & Miller, W. L. (2016). Apparent quantum efficiency spectra for superoxide photoproduction and its formation of hydrogen peroxide in natural waters. *Frontiers in Marine Science*, *3*(NOV). https://doi.org/10.3389/fmars.2016.00235

Rush, J. D., & Bielski, B. H. J. (1985). Pulse radiolytic studies of the reaction of perhydroxyl/superoxide O2- with iron(II)/iron(III) ions. The reactivity of HO2/O2- with ferric ions and its implication on the occurrence of the Haber-Weiss reaction. *The Journal of Physical Chemistry*, *89*(23), 5062–5066. https://doi.org/10.1021/j100269a035

Stedmon, C. A., Markager, S., & Bro, R. (2003). Tracing dissolved organic matter in aquatic environments using a new approach to fluorescence spectroscopy. *Marine Chemistry*, *82*(3–4), 239–254. https://doi.org/10.1016/S0304-4203(03)00072-0

Westerhoff, P., Mezyk, S. P., Cooper, W. J., & Minakata, D. (2007). Electron pulse radiolysis determination of hydroxyl radical rate constants with Suwannee river fulvic acid and other dissolved organic matter isolates. *Environmental Science & Technology*, *41*(13), 4640–4646. https://doi.org/10.1021/es062529n

Wuttig, K., Heller, M. I., & Croot, P. L. (2013). Reactivity of Inorganic Mn and Mn Desferrioxamine B with O2 , O2 – , and H2O2 in Seawater. *Environmental Science & Technology*, *47*(18), 10257–10265. https://doi.org/10.1021/es4016603

Zhang, X., Yin, S., Li, Y., Zhuang, H., Li, C., & Liu, C. (2014). Comparison of greenhouse gas emissions from rice paddy fields under different nitrogen fertilization loads in Chongming Island, Eastern China. *Science of The Total Environment*, *472*, 381–388. https://doi.org/10.1016/J.SCITOTENV.2013.11.014

Zhang, Yi, Del Vecchio, R., & Blough, N. V. (2012). Investigating the Mechanism of Hydrogen Peroxide Photoproduction by Humic Substances. *Environmental Science & Technology*, *46*(21), 11836–11843. https://doi.org/10.1021/es3029582

Zhang, Yunlin, van Dijk, M. A., Liu, M., Zhu, G., & Qin, B. (2009). The contribution of phytoplankton degradation to chromophoric dissolved organic matter (CDOM) in eutrophic shallow lakes: Field and experimental evidence. *Water Research*, *43*(18), 4685–4697. https://doi.org/10.1016/j.watres.2009.07.024